



# Photocatalytic hydrogen evolution from formate and aldehyde over molecular iridium complexes stabilized by bipyridine-bridging organosilica nanotubes



Shengbo Zhang<sup>a</sup>, Mei Li<sup>a</sup>, Qilong Wu<sup>a</sup>, Hongchen Yang<sup>a</sup>, Jinyu Han<sup>a</sup>, Hua Wang<sup>a</sup>, Xiao Liu<sup>b,\*</sup>

<sup>a</sup> Key Laboratory for Green Chemical Technology of the Ministry of Education, School of Chemical Engineering and Technology, Tianjin University, Tianjin 300072, PR China

<sup>b</sup> Key Laboratory of Pesticide & Chemical Biology of the Ministry of Education, College of Chemistry, Central China Normal University, Wuhan 430079, PR China

## ARTICLE INFO

**Keywords:**  
Iridium-bipyridine complex  
Organosilica nanotubes  
Photocatalytic hydrogen evolution  
Formate  
Aldehyde

## ABSTRACT

An efficient heterogeneous photocatalytic system for high-purity hydrogen evolution from formate or aldehyde-water solution were developed using IrCp<sup>\*</sup>Cl (Cp<sup>\*</sup> = η<sup>5</sup>-pentamethylcyclopentadienyl) complex anchored onto the robust bipyridine-based organosilica nanotubes as a solid catalyst. This system can be conducted at the room temperature with a visible light ( $\lambda > 420$  nm) illumination. The heterogeneous molecular photocatalyst displayed much improved catalytic activity and recyclability compared to the analogous homogeneous catalyst, benefiting from the isolated photoactive sites as well as the efficient transport of substrates and products in the nanotube channels. A detailed characterization for the solid catalyst after the reactions by UV-vis, XPS and <sup>13</sup>C CP MAS NMR testified the molecular nature of the active species. This work provides an easy method to construct the heterogeneous molecular photocatalysts for the high-purity hydrogen generation under mild conditions.

## 1. Introduction

The generation of hydrogen (H<sub>2</sub>), one of clean and alternative energy sources [1–6], has been attracted much research attention by using liquid-phase hydrogen storage medium as the starting chemicals [2,4,7–16]. In general, the reaction is carried out at high temperature with the aid of thermal catalysts because the dehydrogenation pathway is thermodynamically favored ( $\Delta G = -48.4$  kJ mol) [17–23]. It is still required to develop efficient and energy-saving methods for hydrogen evolution under mild conditions.

Light-driven chemical reaction is a promising approach to provide renewable energy. Considerable progress has been made on the efficient solid catalyst design over the past few decades [2,24–29]. Compared to inorganic solid catalysts, metal complex molecular catalysts have become a hot research topic owing to the easier mechanistic studies and fine-tuning of molecular structures using synthetic chemistry. For example, as early as 1992, Ziessel reported a Cp<sup>\*</sup>Ir-based (Cp<sup>\*</sup> = η<sup>5</sup>-pentamethylcyclopentadienyl) complex for photocatalytic hydrogen production from formate under acidic conditions [30]. Beller et al. developed an iron carbonyl catalyst for hydrogen evolution (H<sub>2</sub>/CO<sub>2</sub> 1:1) from formic acid with the turnover frequency (TOF) up to 200 h<sup>-1</sup> [31,32]. Very recently, Miller group demonstrated homogeneous

[IrCp<sup>\*</sup>Cl(bpy)]<sup>+</sup> (bpy: 2,2'-bipyridine) complex can produce pure H<sub>2</sub> with TOF of 12 h<sup>-1</sup> from formate under weak basic with a visible light illumination [33], which is the first example of photocatalytic production of pure H<sub>2</sub> from formic acid solutions. The authors further investigated the deactivation pathways of the molecular catalyst, which was caused by the aggregation to form insoluble substances. Considering stability improvement and future practical applications, the immobilization of homogeneous metal complexes on solid supports to isolate the active sites may be a useful strategy for the continuous photocatalytic hydrogen evolution.

Organosilica nanotubes containing various organic functionalities in the frameworks are a new kind of organic-inorganic hybrid solid materials, which possess the distinct properties such as stable structures, high surface areas, confinement effects inside the channels and controllable hydrophobicity/hydrophilicity [34–39]. Several heterogeneous catalytic systems using organosilica nanotubes as the scaffolds were developed in our group [34–38]. Notably, stable AuPd nanocatalysts confined inside amino-functionalized organosilica nanotubes were found to efficiently catalyze visible-light-driven hydrogen evolution from formaldehyde solution [38]. Herein, we report the synthesis of ethenyl-bridged organosilica nanotubes containing bipyridine ligands in the framework (BPy-ENT) to assemble the heterogeneous

\* Corresponding author.

E-mail address: [liuxiao71@tju.edu.cn](mailto:liuxiao71@tju.edu.cn) (X. Liu).

molecular photocatalyst. Through the post-synthetic metalation of BPY-ENT with iridium precursor  $[\text{IrCp}^*\text{Cl}(\mu\text{-Cl})]_2$ , solid catalysts with the structure of  $[\text{IrCp}^*\text{Cl}(\text{bpy})]^+$  were easily prepared and fully characterized by physicochemical analysis. The heterogeneous photocatalysis for hydrogen evolution from formate was conducted under the room temperature with a visible light ( $\lambda > 420 \text{ nm}$ ) illumination, which showed much improved catalytic activity and recyclability compared to the analogous homogeneous one, due to the isolated active species and the suppression of Ir-complex aggregation and decomposition. In addition, we also found the heterogeneous molecular catalyst exhibited efficient catalytic activity for photocatalytic hydrogen evolution from aldehyde-water solution with a visible light ( $\lambda > 420 \text{ nm}$ ) illumination, which has not been reported before.

## 2. Experimental

### 2.1. Materials

4,4'-dimethyl-2,2'-dipyridyl (98%; Aldrich), diisopropylamine (DiPA; > 99.5%; Aladdin), n-butyllithium(n-BuLi; Aldrich; 1.6 M in hexane), pentamethylcyclopentadienyliridium(III) chloride, dimer ( $[\text{Cp}^*\text{IrCl}_2]_2$ ,  $\text{Cp}^*$  is the pentamethylcyclopentadienyl) (96%; Aladdin), (3-chloropropyl)-trimethoxysilane (95%; Heowns), triblock copolymer  $\text{EO}_{20}\text{PO}_{70}\text{EO}_{20}$  (Pluronic P123,  $M_w = 5800$ ), 1,2-bis(trimethoxysilyl)ethane (BTME) and 2,2'-bipyridine were purchased from Sigma-Aldrich Company Ltd. (U.S.A.), and other reagents were obtained from Shanghai Chemical Reagent. 4,4'-(4-(trimethoxysilyl)butyl)-2,2'-bipyridine (bpy-precursor) and  $[\text{IrCp}^*\text{Cl}(\text{bpy})]\text{Cl}$  (Ir-homo) were synthesized according to our previous method [36,37]. All materials were analytical grade and used without any further purification.

### 2.2. Synthesis of bipyridine- and ethenyl-bridging bifunctional organosilica nanotubes

In a typical synthesis, 0.55 g of P123 and 1.75 g of KCl were dissolved in 150 ml 2 M HCl solution at 38 °C. After the copolymer was fully dissolved, 3.15 mmol of 1,2-bis(trimethoxysilyl)ethane (BTME) was added with vigorous stirring 6 min. After stirring for 12 h at 38 °C, 0.35 mmol of bpy-precursor was added dropwise. The molar ratio of BTME to bpy-precursor in the resulting mixture was 9:1. Then the mixture was stirred at 38 °C for 24 h and the resultant mixture was transferred to a PTFE hydrothermal reactor at 100 °C for an additional 24 h. The solid product was recovered by filtration, washed with distilled water thoroughly and dried at room temperature overnight. Finally, the surfactant was extracted by refluxing 1.0 g of the as-synthesized material in 200 ml of ethanol containing 1.27 g concentrated HCl for 24 h. The obtained sample was denoted as BPY-ENT, where BPY, E and NT represented bipyridine, ethenyl and nanotube, respectively.

### 2.3. Post-synthetic metalation of BPY-ENT with Ir complex

Dried BPY-ENT (100 mg) was added to a solution of  $[\text{Cp}^*\text{IrCl}(\mu\text{-Cl})]_2$  (10 mg) in 60 ml of anhydrous ethanol under an nitrogen atmosphere. After the suspension was stirred under refluxing conditions for 24 h, the solid phase was removed by filtration and washed with distilled water and DMF to remove any unreacted Ir precursor. The final Ir-based organosilica nanotubes were named as Ir-BPY-ENT. As comparison, Ir complex was also incorporated onto bipyridine-bridging silica nanotubes without ethenyl groups (Supporting information), denoting as Ir-BPY-SNT.

### 2.4. Characterization

Transmission electron microscopy (TEM) were operated on a JEM-2100 F system operating at 200 kV. The morphology of the materials were analyzed by scanning electron microscopy (SEM) using Hitachi S-

4800 scanning electron microscope (SEM, 5 kV) equipped with the Thermo Scientific energy-dispersion X-ray fluorescence analyser. UV/vis absorption and diffuse reflectance spectra were obtained using Instant Spec BWS003 spectrometers.  $N_2$  adsorption-desorption isotherms were tested at  $-196^\circ\text{C}$  on a Micromeritics Tristar 3000 instrument. The specific surface areas were obtained by the Brunauer–Emmett–Teller method. The pore size distribution was obtained by the Barrett–Joyner–Halenda method using the adsorption branch. X-ray photoelectron spectroscopy (XPS) was carried out on a PHI 1600 (PerkinElmer). All spectra were recorded at the room temperature and the binding energy was referred to C 1s peak at 284.8 eV. FT-IR spectra were collected with a Bruker Vertex 80v. Carbon, hydrogen and nitrogen contents were determined via CHN elemental analysis (vario EL CUBE). Solid-state  $^{13}\text{C}$  and  $^{29}\text{Si}$  dipolar decoupling magic angle spinning (DD-MAS) NMR spectra were collected on Infinityplus 300 instruments. Solution  $^1\text{H}$  NMR and  $^{13}\text{C}$  NMR spectra were recorded on a Mercury VX 400 MHz instrument. Photocurrent responses were operated on a Autolab 302N instrument.

### 2.5. Hydrogen evolution from formate solution

In a typical experiment, Ir-BPY-ENT was added to a fresh  $\text{HCOONa}$  solution ( $\text{pH} = 9$ , 50 mL, 1 M  $\text{HCOONa}$ , 0.18 mM Ir) was purged with  $N_2$  for 0.5 h. The reaction was operated at the room temperature with a visible light ( $\lambda > 420 \text{ nm}$ ) illumination. The  $\text{H}_2$  molecules generated in the head space were periodically analyzed quantitatively by a Bruker 456 gas chromatograph equipped with a thermal conductivity detector (TCD). For the recycling catalytic performance, the catalyst was recovered by simple filtration after every 5 h, dried and used for the next run.

### 2.6. Hydrogen evolution from aldehyde base solution

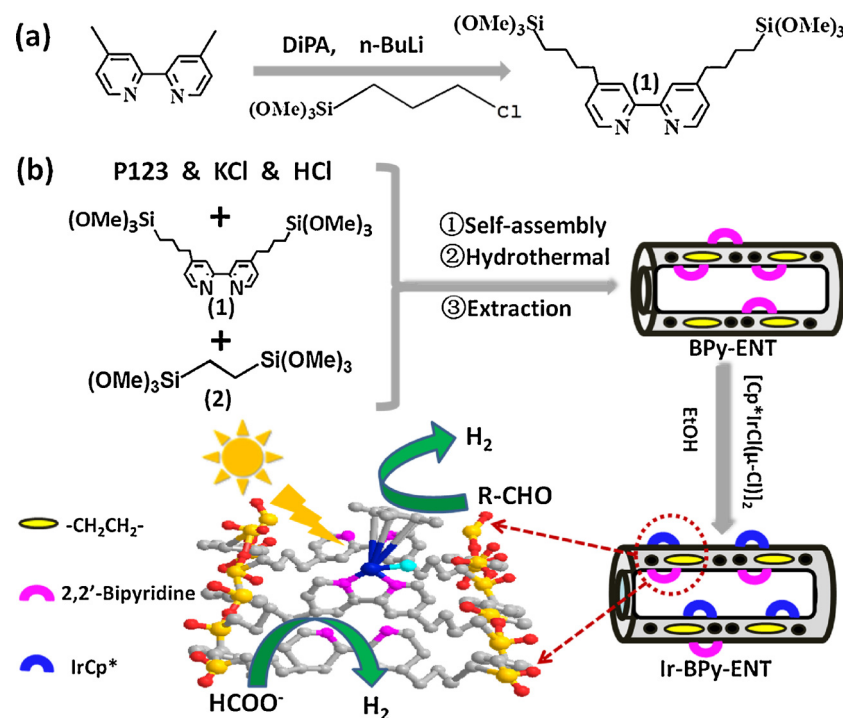
In a typical experiment, Ir-BPY-ENT was added to a fresh aldehyde-water base solution (1 M  $\text{HCHO}$ , 1.0 M  $\text{NaOH}$ , 50 mL, 0.18 mM Ir) was purged with  $N_2$  for 0.5 h. The reaction was operated at the room temperature with a visible light ( $\lambda > 420 \text{ nm}$ ) illumination. The  $\text{H}_2$  molecules generated in the head space were periodically analyzed quantitatively by a Bruker 456 gas chromatograph equipped with a thermal conductivity detector (TCD).

## 3. Results and discussion

### 3.1. Synthesis of two kinds of bipyridine-bridging organosilica nanotubes (BPY-ENT and BPY-SNT)

The bipyridine precursor (1) was prepared according to our previous method [36] in Scheme 1a. The bipyridine- and ethenyl-incorporated bifunctional organosilica nanotubes (BPY-ENT) were synthesized by the hydrolysis and co-condensation of bpy-precursor (1) and 1,2-bis(trimethoxysilyl)ethane (2) under acid conditions with triblockcopolymer  $[(\text{EO})_{20}(\text{PO})_{70}(\text{EO})_{20}]$ , P123] as a soft template, followed by the extraction of templates with an acidic ethanol solution. Meanwhile, as a comparison, the bipyridine-incorporated organosilica nanotubes without ethenyl in the frameworks (BPY-SNT) were also synthesized by using the similar soft-template strategy, except for the replacement of precursor (2) with tetraethyl orthosilicate (TEOS).

Fig. 1 shows transmission electron microscopy (TEM) and scanning electron microscopy (SEM) images of BPY-ENT and BPY-SNT, respectively. We can clearly see from the TEM images that the bipyridine- and ethenyl-bridging bifunctional organosilicas (BPY-ENT) are composed of nanotubes with the inner diameter of  $\sim 6 \text{ nm}$  and wall thickness of  $\sim 3 \text{ nm}$  (Fig. 1a). The SEM image further confirms that these nanotubes have been large-scaley synthesized (Fig. 1c). The bipyridine-incorporated organosilicas BPY-SNT with bpy-precursor and TEOS as the silanes exhibit the similar nanotube structures with the diameter of



**Scheme 1.** Synthetic routes and photocatalysis of molecular heterogeneous catalyst based on organosilica nanotubes.

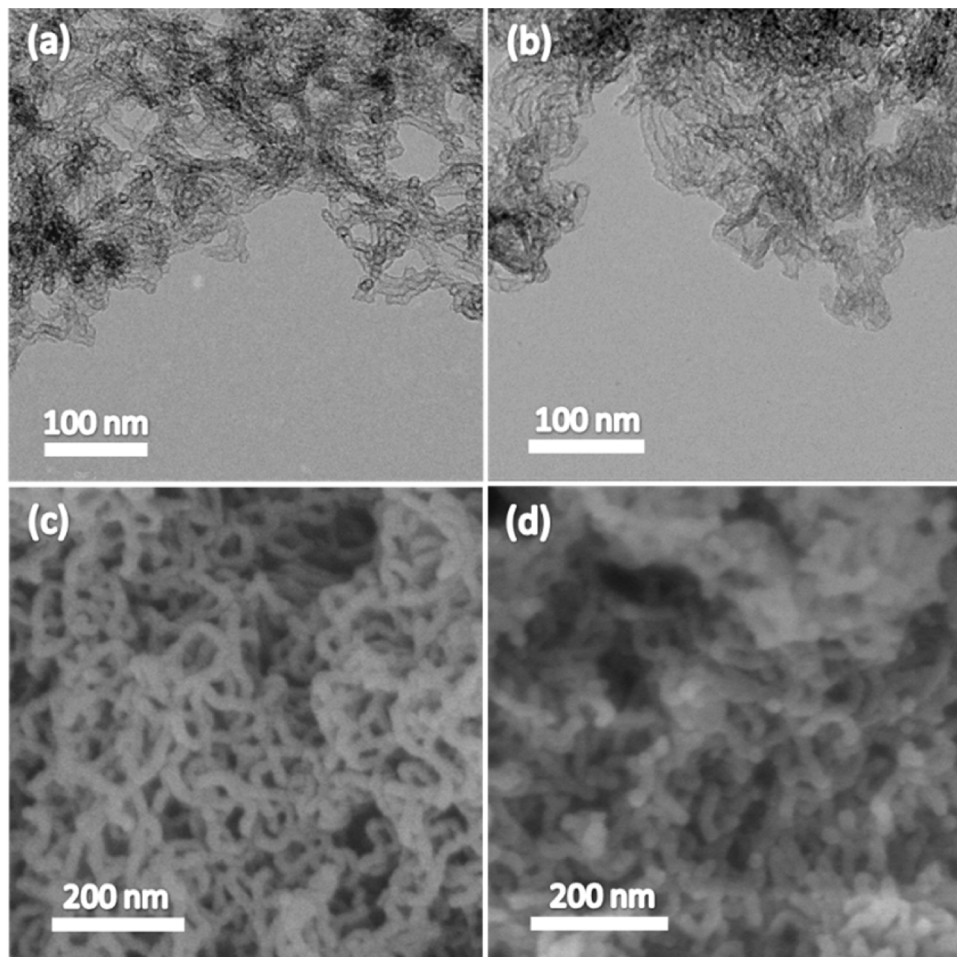


**Fig. 1.** (a,b) TEM and (c,d) SEM images of (a,c) BPy-ENT, (b,d) BPy-SNT.

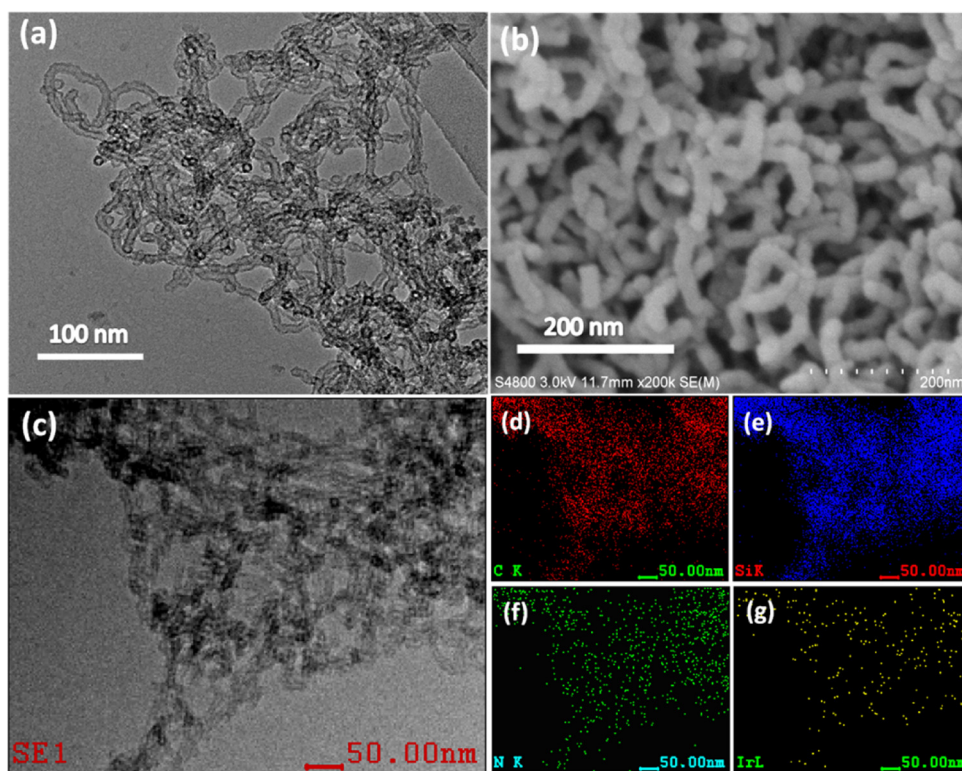


**Fig. 2.** (a) TEM, (b) SEM, (c) Dark field STEM image and (d–g) the elemental mapping images of Ir-BPy-ENT: (d) C, (e) Si, (f) N and (g) Ir.

~7 nm from TEM image (Fig. 1b).

The nitrogen adsorption-desorption isotherms of BPy-ENT and BPy-SNT were type IV with a hysteresis loop at relative pressure  $P/P_0 = 0.5\text{--}0.7$ , which are typical for mesoporous materials (Figs. 3a and S5). The pore diameter and BET surface areas were shown and summarized in Figs. S1, S5 and Table S1. It can be seen that the pore diameters of BPy-ENT and BPy-SNT are 6.8 and 7.6 nm, respectively, consistent with TEM results. What is more, both of the nanotube materials display high surface areas with about  $700 \text{ m}^2/\text{g}$ , which is beneficial for the heterogeneous catalysis as the scaffolds.

### 3.2. Synthesis of molecular iridium complexes immobilized by bipyridine-bridging organosilica nanotubes (Ir-BPy-ENT and Ir-BPy-SNT)

The direct immobilization of an iridium-Cp\* complex on the nanotube walls were prepared by adding BPy-ENT or BPy-SNT to a solution of  $[\text{IrCp}^*\text{Cl}(\mu\text{-Cl})]_2$  in anhydrous ethanol under nitrogen atmosphere and the dried samples were named as Ir-BPy-ENT and Ir-BPy-SNT, respectively. After the postsynthetic metalation of Ir complex, the nanotube structure was kept from TEM and SEM characterization in Figs. 2 and S4. Fig. 2d–g and Fig. S4(c–f) show the energy-dispersive X-ray spectrometry (EDX) mapping analysis of the chosen area, which indicated that Ir was uniformly distributed on the support. EDX shows the Ir loadings were 0.18 and 0.20 mmol/g for Ir-BPy-ENT and Ir-BPy-SNT, respectively, which was also confirmed by inductively coupled plasma (ICP) measurement. Combined with CHN elemental analysis, the Ir/bpy molar ratios were determined to be 0.37 and 0.39, respectively.

The nitrogen adsorption-desorption isotherms of Ir-BPy-ENT and Ir-BPy-SNT were type IV with a hysteresis loop at relative pressure  $P/P_0 = 0.5\text{--}0.7$ , which are typical for mesoporous materials (Figs. 3a and S5). The textural properties of these samples are summarized in Table S1. These results further demonstrate the maintenance of the nanotube structure of BPy-ENT and BPy-SNT after the immobilization of the iridium complex. The pore diameter and BET surface area were found to be slightly decreased after the formation of the iridium complex on BPy-

ENT and BPy-SNT, as shown in Figs. 3a and S5. These phenomena can be attributed to iridium complex inside the channels of the BPy-ENT and BPy-SNT, which leads to a partial blocking of the channels.

The formation of  $[\text{IrCp}^*\text{Cl}(\text{bpy})]^+$  on BPy-ENT was confirmed by UV-vis diffuse reflectance spectrometry and solid-state  $^{13}\text{C}$  cross polarization magic-angle spinning (CP MAS) NMR spectroscopy. Fig. 3b shows the UV-vis absorption spectra of the BPy-ENT and Ir-BPy-ENT. For BPy-ENT, there is one main absorption peak at around 290 nm, corresponding to the absorption of bipyridine groups. After the postsynthetic metalation of Ir, two new metal-to-ligand charge transfer (MLCT) absorption bands (around 370 and 450 nm) appeared, assignable to the coordination of Ir to bipyridine ligand, same with homogeneous complex  $[\text{IrCp}^*\text{Cl}(\text{bpy})]\text{Cl}$  (denoted as Ir-homo).

In addition, the solid-state  $^{13}\text{C}$  cross polarization magic-angle spinning (CP MAS) NMR spectroscopy (Fig. 3c) shows small signal peaks at 120–165 ppm, which belonged to bipyridine groups. The peaks at 10, 27, 35, 48 ppm were attributed to alkyl groups of bipyridine precursors (1). The strong peak at 5.7 ppm attributed to C in  $-\text{CH}_2\text{CH}_2-$  groups from 1,2-bis(trimethoxysilyl)ethane (2). The two new signals at 9 and 90 ppm are assignable to the Cp\* ligand of Ir-complex in Ir-BPy-ENT. The signals at 16, 58 ppm were due to the carbons of the ethoxy groups formed during the ethanol treatment for removal of the surfactant. The  $^{29}\text{Si}$  MAS NMR spectrum of Ir-BPy-ENT (Fig. S3) showed two resonance peaks at  $-62$ ,  $-71$  ppm, which were assigned to silicon species  ${}^2\text{T} [\text{SiC(OH)(OSi)}_2]$  and  ${}^3\text{T} [\text{SiC(OSi)}_3]$ , respectively. What is more, the X-ray photoelectron spectroscopy (XPS) of Ir-BPy-ENT is in good agreement with that of Ir-homo (Fig. 3d), which strongly indicated the successful formation of the iridium complex  $[\text{IrCp}^*\text{Cl}(\text{bpy})]^+$  on the nanotubes. These above results fully indicated the successful synthesis of the heterogeneous molecular solid  $[\text{IrCp}^*\text{Cl}(\text{bpy})]^+$  on bipyridine-bridging organosilica nanotubes BPy-ENT.

The optical properties of Ir-BPy-ENT were further measured by photoluminescence (PL) spectroscopy and photocurrent responses as shown in Fig. 4. PL spectroscopy (Fig. 4a) of Ir-BPy-ENT exhibited a lower PL intensity than those of Ir-homo, Ir-BPy-SNT and BPy-ENT with

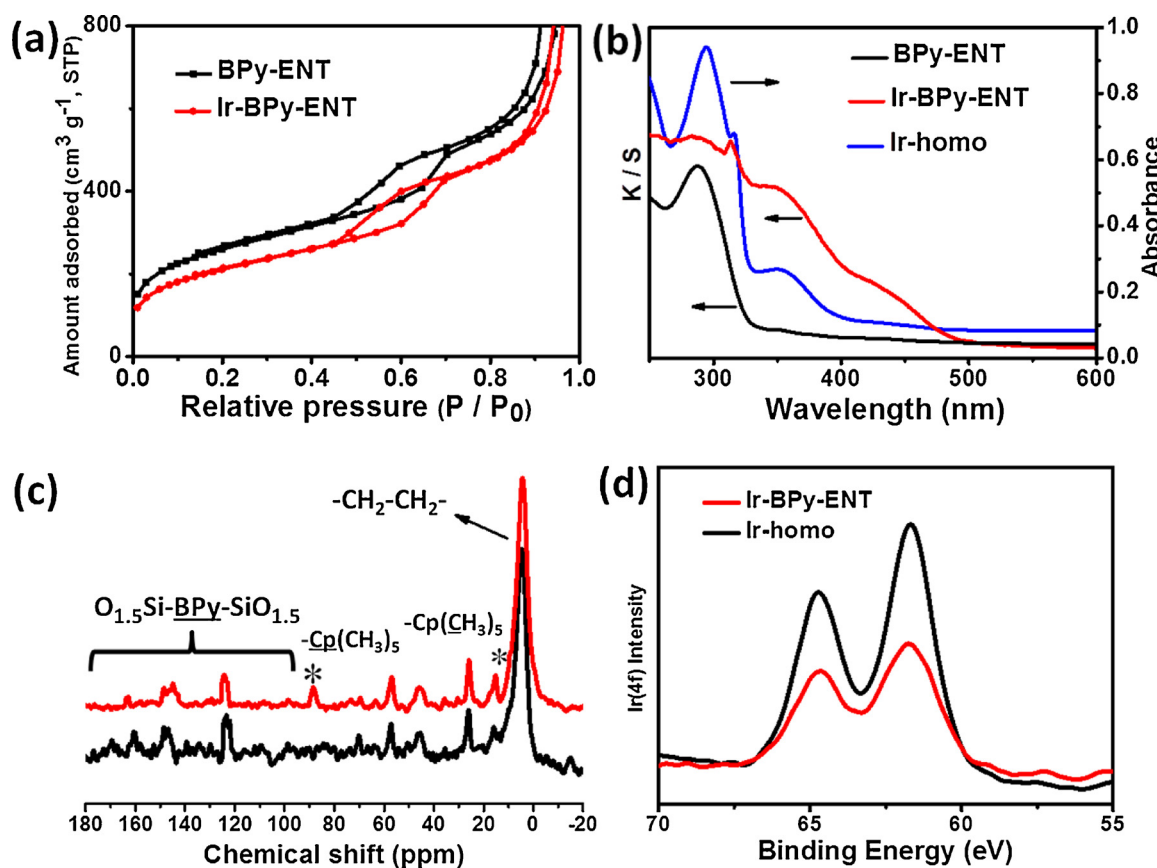


**Fig. 3.** (a) Nitrogen adsorption-desorption isotherms, (b) UV/vis diffuse reflectance spectra, (c) <sup>13</sup>C CP MAS NMR spectra of BPY-ENT (black line) and Ir-BPy-ENT (red line), and (d) the XPS spectra of Ir-homo (black line) and Ir-BPy-ENT (red line) (For interpretation of the references to colour in this figure legend, the reader is referred to the web version of this article).

a peak centered at 465 nm irradiated by a 340 nm laser, which can be attributed to the efficient photoinduced charge transfer process. The PL result demonstrates that the heterogeneous molecular Ir-BPy-ENT has a good blue light-emitting property.

In addition, the photocurrent ( $I_{ph}$ ) generation performance of heterogeneous molecular Ir-BPy-ENT was investigated to illustrate the photoinduced charge transfer and separation efficiency. As shown in Fig. 4b, the photocurrent density of Ir-BPy-ENT electrode under visible light ( $\lambda > 420$  nm) irradiation is about  $7.5 \mu\text{A}/\text{cm}^2$ . More importantly, the heterogeneous molecular Ir-BPy-ENT exhibited stronger

photocurrents responses compared to Ir-BPy-SNT, BPY-ENT and the homogeneous Ir-homo. The enhancement of  $I_{ph}$  indicates the efficient photogenerated charge transfer and separation in Ir-BPy-ENT. The superior photoelectronic property may be favorable to promote the photocatalytic activity.

### 3.3. Catalytic performance of heterogeneous molecular catalysts for visible-light-driven hydrogen evolution from formate solution

Subsequently, the photocatalytic hydrogen evolution activity of Ir-

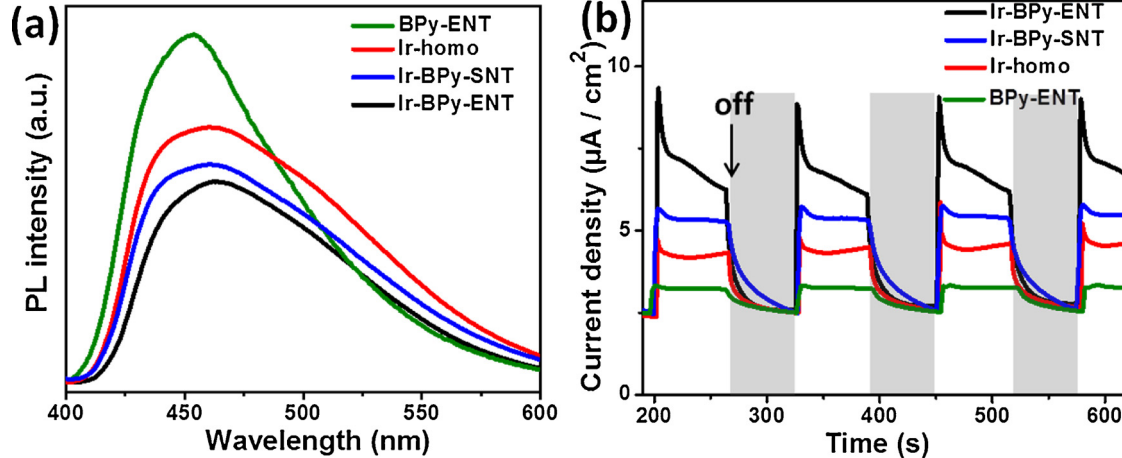


**Fig. 4.** (a) Photoluminescence (PL) spectrum of the Ir-BPy-ENT, Ir-BPy-SNT, BPY-ENT and Ir-homo stimulated by 340 nm laser. (b) Photocurrent responses of Ir-BPy-ENT, Ir-BPy-SNT, BPY-ENT and Ir-homo casted on FTO glass vs. Ag/AgCl in a 1.0 M formate buffer solution.

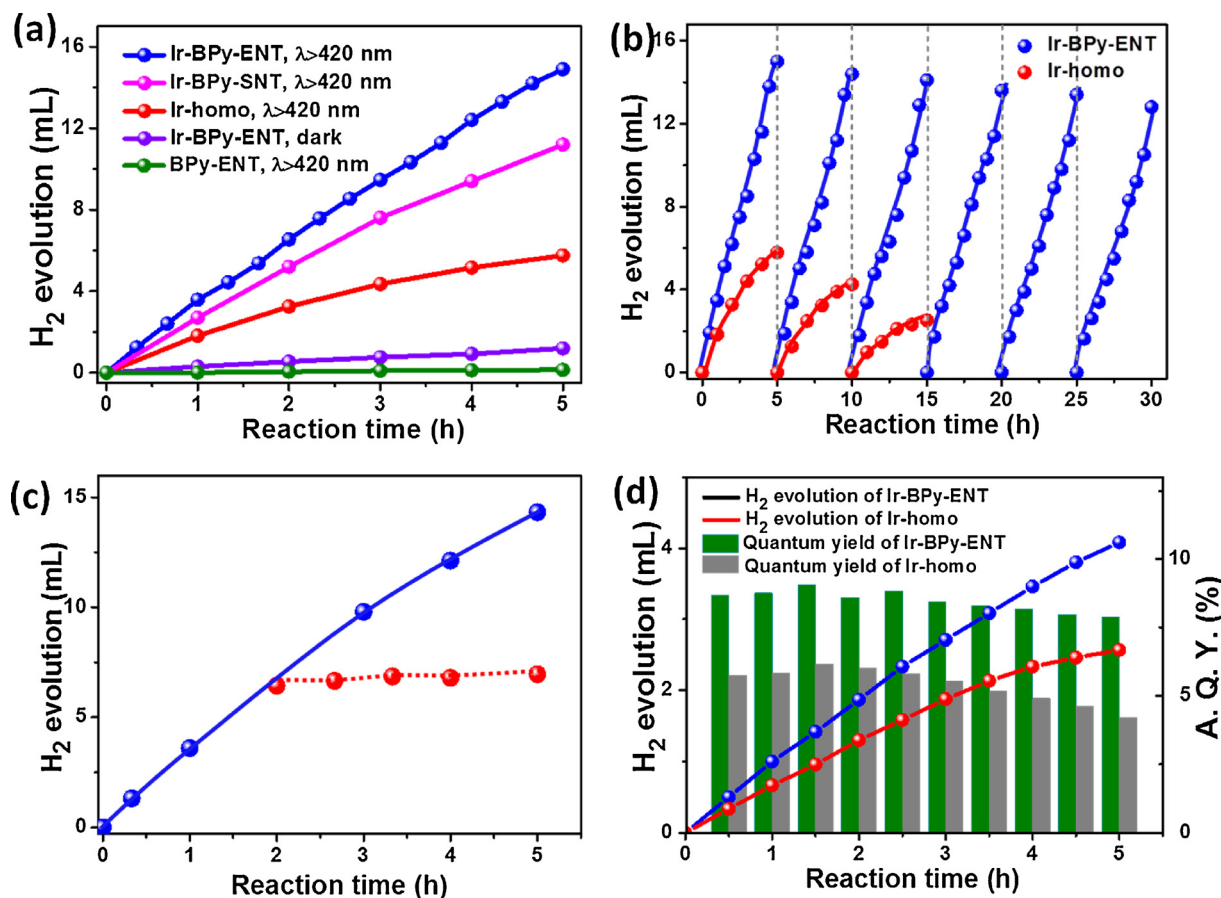


**Fig. 5.** (a) Time-dependent hydrogen evolution curves from formate of the Ir-BPy-ENT, Ir-BPy-SNT, BPY-ENT and Ir-homo. (b) The recycling performance of Ir-BPy-ENT for hydrogen evolution from 1 M formate (0.18 mM Ir). (c) The filtration test of Ir-BPy-ENT for hydrogen evolution from 1 M formate (0.18 mM Ir). (d) Kinetic curves of hydrogen evolution and apparent quantum yield on Ir-BPy-ENT photocatalyst under monochromatic 435 nm light irradiation (1 M formate, 0.18 mM Ir).

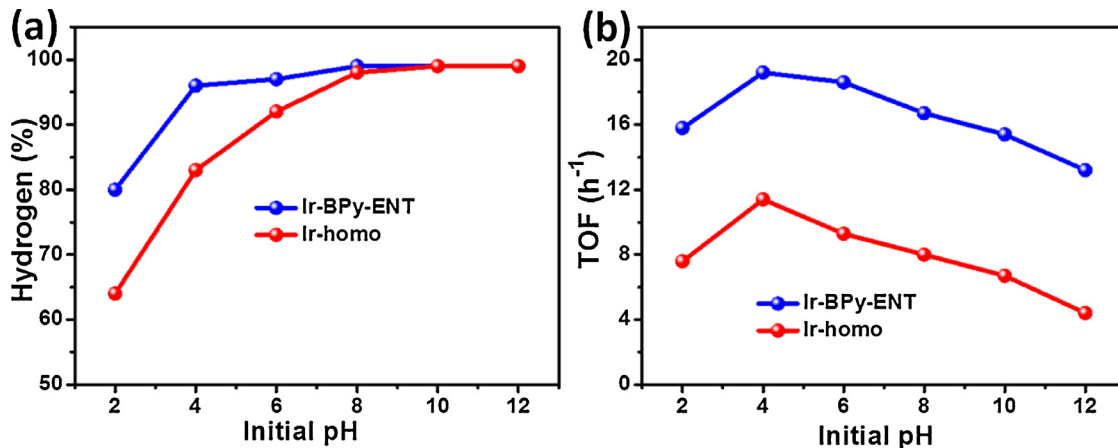


**Fig. 6.** Effects of initial pH on (a) the hydrogen purity and (b) initial TOF (according to the H<sub>2</sub> produced within 2 h) from formate under visible light irradiation ( $\lambda > 420$  nm) for the Ir-BPy-ENT and Ir-homo.

based heterogeneous molecular catalysts was tested in a 50 mL of 1.0 M formate solution containing 0.18 mM Ir under mild conditions [weakly basic solution (pH = 9) at room temperature] (Fig. 5a). The solution of Ir-BPy-ENT generated negligible amounts of gas in the dark. However, under a visible light ( $\lambda > 420$  nm) irradiation, the solution containing Ir-BPy-ENT catalyst produced 14.9 mL H<sub>2</sub> in 5 h with an initial TOF of 16.2 h<sup>-1</sup> based on the amounts of hydrogen produced per unit of Ir. More importantly, the evolved gas is comprised of ~100% H<sub>2</sub> due to the efficient sequestration of CO<sub>2</sub> by hydroxide under basic conditions, which was also confirmed by the previous report [33]. No hydrogen

was generated in the presence of only BPY-ENT without Ir loading under the visible light irradiation (Fig. 5a). As comparison, we synthesized IrCp\*Cl(bpy) on organosilica nanotubes without  $-\text{CH}_2\text{CH}_2-$  in the framework. It can be seen that Ir-BPy-SNT produced lower H<sub>2</sub> amount (11.2 mL) in 5 h with a lower initial TOF of 12.9 h<sup>-1</sup> than Ir-BPy-ENT. The higher activity of Ir-BPy-ENT may be attributed to that the existence of  $-\text{CH}_2\text{CH}_2-$  in the framework of organosilica nanotubes can efficiently accelerate the desorption of the by-product HCO<sub>3</sub><sup>-</sup> from the catalytic active center and promote the reaction. This result further indicates the heterogeneous catalytic activity can be adjusted through

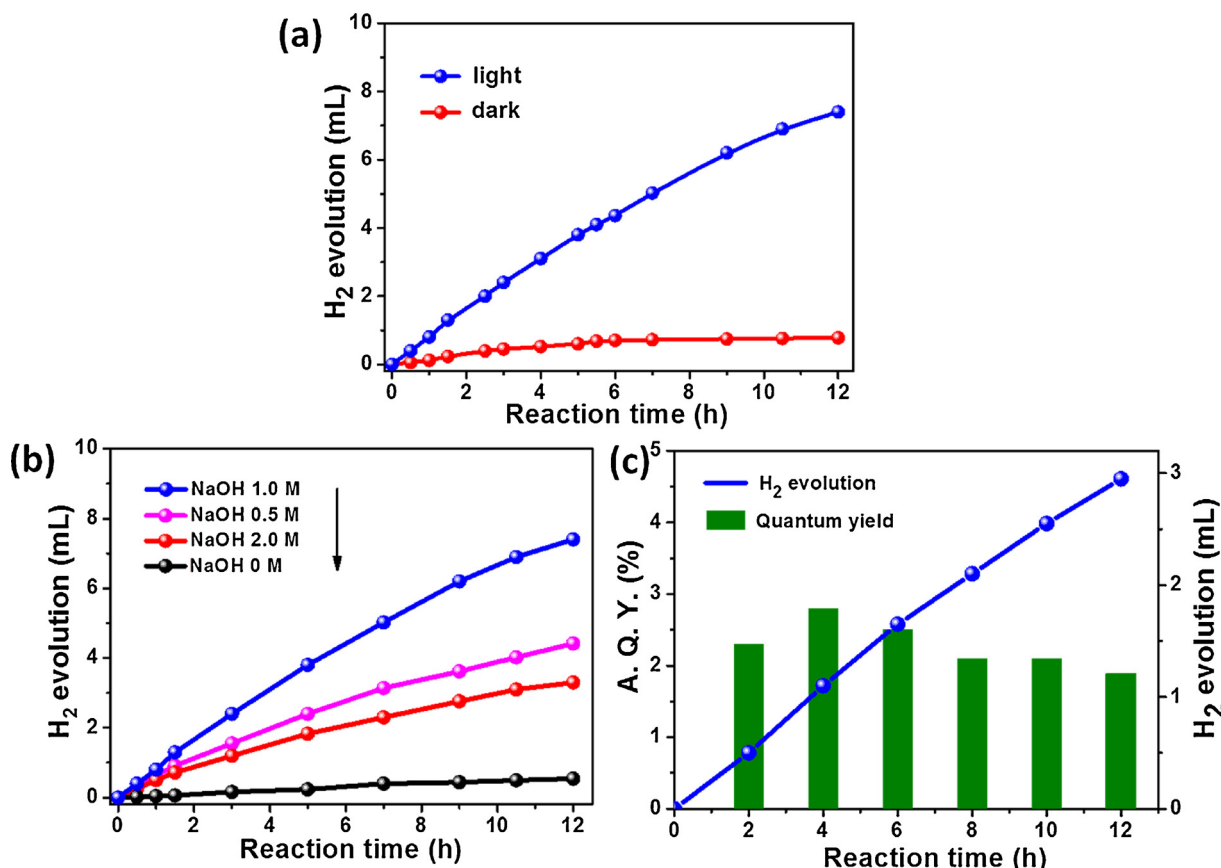


**Fig. 7.** (a) Kinetic curves of Ir-BPy-ENT for hydrogen evolution from 1.0 M formaldehyde-water solution, (b) effect of NaOH concentration on the hydrogen evolution from formaldehyde under visible light irradiation ( $\lambda > 420$  nm) for Ir-BPy-ENT and (c) kinetic curves of hydrogen evolution and apparent quantum yield on Ir-BPy-ENT and Ir-homo photocatalyst under monochromatic 435 nm light irradiation (1 M formaldehyde-water solution, 0.18 mM Ir).

**Table 1**  
Ir-BPy-ENT-catalyzed hydrogen evolution from different substrates.

Reagents	Reaction time/h	H <sub>2</sub> Volume/mL	
		dark	light
HCHO	12	0.7	7.4
CH <sub>3</sub> CHO	20	0	2.9
CH <sub>3</sub> CH <sub>2</sub> CHO	20	0	1.6
C <sub>6</sub> H <sub>5</sub> CHO	20	0	4.2

Conditions: 0.18 mM Ir, 1.0 M reagents, 298 K,  $\lambda > 420$  nm.

the regulation of the microenvironment around the active species.

On the contrary, the homogeneous catalyst [IrCp<sup>\*</sup>Cl(bpy)]Cl (Ir-homo) provided only 5.8 mL H<sub>2</sub> within 5 h under the same reaction conditions, one third of H<sub>2</sub> amount generated by Ir-BPy-ENT. Moreover, with the increasing of the reaction time, the reaction rate of Ir-homo showed a gradual decrease. Miller has reported that Ir-homo may undergo the deactivation and/or decomposition processes due to the unfavourable aggregation Ir active centers [33]. Under our reaction conditions, after 10 h of the reaction, the initial yellow color of the homogeneous solution produced black solid precipitates (Fig. S9). Unexpectedly, by the analysis of TEM and EDX (Fig. S10), the uniform and highly dispersed solid precipitates are composed of Ir nanoparticles with the average size of 2–4 nm, which provided us a simple photochemical method for the *in situ* synthesis of ultrafine Ir nanoparticles. Furthermore, the Mass Spectrum (MS) was used to detect the structure of the homogeneous catalyst (Fig. S11). It reveals that the peak of [IrCp<sup>\*</sup>Cl(bpy)]Cl at 519.1182 disappeared, indicating that the homogeneous catalyst has been totally decomposed. The time-dependent

hydrogen evolution curve further confirmed the total deactivation of Ir-homo after 10 h. However, hydrogen was continuously generated over Ir-BPy-ENT even after 20 h (Fig. S12).

The reusability experiment was performed at 5 h intervals to confirm the photocatalytic activity and stability of Ir-BPy-ENT under visible light irradiation. After the reaction, Ir-BPy-ENT was recovered by simple filtration and reused for the next run. As shown in Fig. 5b, there was no significant decrease in H<sub>2</sub> evolution even after the 6th cycle. After the recycle, the solid catalyst was removed from the reaction system and the solid-free solution was colorless (Fig. S13), indicating the Ir active species was coordinated firmly with BPy-ENT. Inductively coupled plasma optical emission spectroscopy (ICP-OES) confirmed no leaching of Ir species in the filtrate. In contrast, the homogeneous one showed a gradual decrease in H<sub>2</sub> yield after the first recycle (Fig. 5b). The comparison in the activity and durability between Ir-BPy-ENT and Ir-homo fully demonstrated the aggregation of the iridium-bipyridine complex could be suppressed through the isolation of the active centers. In addition, the filtration experiment was conducted to further check the heterogeneity and stability of the solid catalyst (Fig. 5c). After the reaction system was stirred for 2 h, the solid catalyst was filtered off from the reaction mixture, and the remaining solution continued to stir for another 3 h. The volume of H<sub>2</sub> has no significant increase, indicating that the reaction completely ceased and the catalytic activity came from Ir-BPy-ENT.

The analysis on the recovered solid heterogeneous catalysts by TEM, SEM, EDX mapping and nitrogen adsorption-desorption analysis (Figs. S14–16) indicated the nanotube structure was kept and the Ir was uniformly distributed on the support after the 6th reaction. UV-vis and <sup>13</sup>C CP MAS NMR (Figs. S17, S18) show the firm coordination of Ir with bipyridine ligands and the intact structure of the active site IrCp<sup>\*</sup>Cl

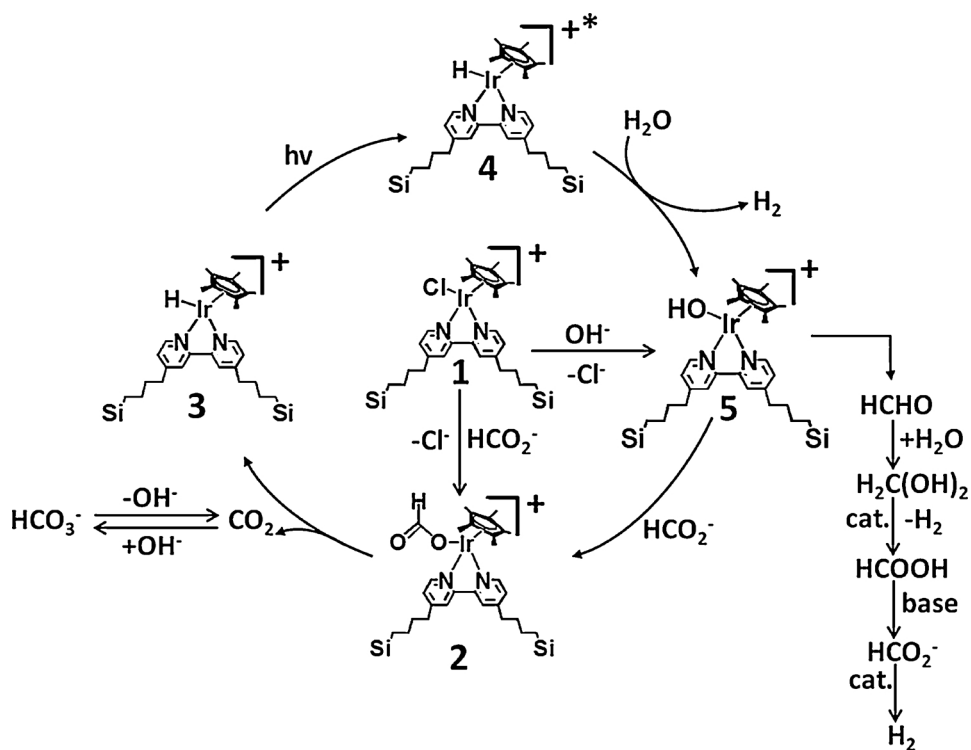


Fig. 8. Proposed mechanism of photochemical hydrogen evolution from formic acid and formaldehyde.

(bpy), respectively.  $^{29}Si$  MAS NMR spectrum shows that the silica framework containing ethenyl and bipyridine was quite stable during the reaction (Fig. S19). Furthermore, XPS reveals the valence state of Ir after the reaction was kept at III (Fig. S20).

The apparent quantum yield ( $\Phi$ : defined as the moles of  $H_2$  produced divided by the moles of incident photons) for  $H_2$  evolution was tested in a 50 mL of 1.0 M formate solution containing 0.18 mM Ir at the room temperature. The solution was irradiated by monochromatic 435 nm visible light irradiation and the results are shown in Fig. 5d. The apparent quantum yield (~8.0%) maintained over the course of 5 h for Ir-BPy-ENT. As a comparison, the homogeneous Ir-homo gave a lower apparent quantum yield (~5.0%) with a gradual decrease of catalytic activity, owing to the aggregation and decomposition of Ir active centers.

The effect of pH on the hydrogen evolution performance was investigated by using the Ir-BPy-ENT catalyst. As shown in Fig. 6a, the hydrogen purity was ~80% in the evolved gas with ~20%  $CO_2$  (no  $CO$  detected) at pH = 2. When the pH of solution was increased to 4 from 2, the purity of hydrogen was increased obviously from 80% to 96%. Above the pH of 4, the hydrogen purity was ~100% in the evolved gas. However, the purity of hydrogen for homogeneous Ir-homo is lower than that of Ir-BPy-ENT below pH 8, which is mainly attributed to the strong  $CO_2$  adsorption of the residual bipyridine ligands in the frameworks of organosilica nanotubes [40]. On the other hand, the hydrogen evolution rate for Ir-BPy-ENT catalyst depends largely on the pH of reaction system (Fig. 6b). When the pH of solution was increased to 4 from 2, the TOF of hydrogen have been increased from 15.8 to 19.2  $h^{-1}$  under the visible light illumination ( $\lambda > 420$  nm). When further increasing the pH of solution to 12, the TOF of  $H_2$  has been gradually decreased ( $13.2\text{ }h^{-1}$ ). Ir-homo has the same tendency. The above results indicate that the pH of the system has a great influence on hydrogen evolution from formate solution.

#### 3.4. Catalytic performance of Ir-BPy-ENT catalysts for visible-light-driven hydrogen evolution from formaldehyde-water solution

Recently, we found that PdAu nanoclusters confined inside amino-functionalized organosilica nanotubes can catalyze visible-light-driven hydrogen evolution from formaldehyde solution [38]. In order to explore more applications of molecular-based solid Ir-BPy-ENT, we further tried the dehydrogenation of formaldehyde-water solution with a visible light ( $\lambda > 420$  nm) illumination at the room temperature. As shown in Fig. 7a, only trace hydrogen gas been been detected in the dark. On the contrary, the hydrogen evolution reaction occurred immediately under the visible light illumination, indicating that the light is indispensable for this catalytic process. Within 12 h, the generated hydrogen reached to 7.4 mL. Notably,  $H_2$  production from formaldehyde-water solution by using molecular-based solid photocatalyst has not been reported yet as far as we know. On the other hand, the hydrogen evolution rate for Ir-BPy-ENT catalyst depends largely on the concentration of NaOH (Fig. 7b). For example, when the concentration of NaOH was increased from 0 to 1.0 M, the volume of hydrogen have been increased obviously from 0.5 to 7.4 mL at 12 h in a 50 mL of 1.0 M formaldehyde-water solution containing 0.18 mM Ir under a visible light illumination. However, when further increasing the concentration of NaOH to 2.0 M, the volume of  $H_2$  has decreased obviously, which was attributed to the transformation of formaldehyde into methanol in highly alkaline conditions [38,41,42]. The apparent quantum yield ( $\Phi$ ) for  $H_2$  evolution was also tested in a 50 mL of 1.0 M formaldehyde-water solution containing 0.18 mM Ir with monochromatic 435 nm visible light irradiation at room temperature (Fig. 7c). The apparent quantum yield (~2.0%) maintained over the course of 12 h, indicating the high stability of Ir-BPy-ENT under the photocatalytic conditions.

Besides formaldehyde, other aldehydes, including acetaldehyde, propanal and benzaldehyde are also investigated to produce hydrogen gas. As shown in Table 1, the  $H_2$  amounts from acetaldehyde, propanal and benzaldehyde were 2.9, 1.6 and 4.2 mL within 20 h, respectively. For the acetaldehyde and propanal, the electron density of carbon in  $-CHO$  is higher than that of formaldehyde and benzaldehyde.

Therefore, it is harder to be attacked by  $\text{OH}^-$  to form aldehydrol, leading to the decrease in hydrogen evolution amount.

A possible photocatalytic mechanism for hydrogen evolution from formate is presented in Fig. 8. Firstly, the photocatalyst 1 would be converted into species 2 in the basic formate solution. And then the species 2 was decomposed into species 3 under the basic conditions. Subsequently, the species 3 quickly converted into the excited state species 4 under the visible light ( $\lambda > 420 \text{ nm}$ ) illumination, which is the real photocatalytic active species according to the previous report [33,43]. The degradation pathway was efficiently suppressed through the isolation of the species 4 on the nanotubes. Finally, the active species 4 interacted with the water and then  $\text{H}_2$  was released. For the hydrogen evolution from formaldehyde-water solution, a possible reaction pathway was proposed. First, the formaldehyde in the water can be totally hydrated to form methylene glycol, and then methylene glycol was catalyzed by photocatalyst in the basic conditions to give hydrogen and formic acid [19]. The subsequent process is the dehydrogenation of formic acid in basic conditions.

#### 4. Conclusions

In summary, we have developed a novel and efficient heterogeneous photocatalytic system for the hydrogen production from formate and aldehyde-water solution by using  $[\text{IrCp}^*\text{Cl}(\text{bpy})]$  complex anchored onto the highly robust bipyridine-based organosilica nanotubes. The aggregation of molecular photocatalyst could be efficiently inhibited through the isolation of the active species, resulting in the enhanced activity and stability for the  $\text{H}_2$  production. Furthermore, this system can be conducted under mild conditions (visible light illumination, weakly basic solution and room temperature). Especially, it is the first time to report the hydrogen production from aldehyde-water solution by using molecular-based photocatalyst. Moreover,  $\text{H}_2$  was the only gaseous product in this system and CO was not generated, which can greatly meet the criteria of hydrogen production from the angle of safety and purity, especially for proton exchange membrane fuel cells. We believe that Ir-BPy-ENT is promising as a rigid heterogeneous molecular photocatalyst for hydrogen evolution reaction and it provides an integration platform for the assembly of metal complexes in artificial photosynthesis systems.

#### Notes

The authors declare no competing financial interest.

#### Acknowledgments

We acknowledge the National Natural Science Foundation of China (U1662109), the Natural Science Foundation of Tianjin, China (16JCQNJC06200) for financial support. The Program of Introducing Talents of Discipline to Universities of China (111 program, B17019) is also acknowledged.

#### Appendix A. Supplementary data

Supplementary material related to this article can be found, in the online version, at doi: <https://doi.org/10.1016/j.apcatb.2018.05.058>.

#### References

- [1] Y.J. Yuan, Z.T. Yu, D.Q. Chen, Z.G. Zou, Chem. Soc. Rev. 46 (2017) 603–631.
- [2] D. Mellmann, P. Sponholz, H. Junge, M. Beller, Chem. Soc. Rev. 45 (2016) 3954–3988.
- [3] Y. Shi, B. Zhang, Chem. Soc. Rev. 45 (2016) 1529–1541.
- [4] S. Fukuzumi, Y. Yamada, T. Suenobu, K. Ohkubo, H. Kotani, Energy Environ. Sci. 4 (2011) 2754–2766.
- [5] J. Willkomm, K.L. Orchard, A. Reynal, E. Pastor, J.R. Durrant, E. Reisner, Chem. Soc. Rev. 45 (2016) 9–23.
- [6] M. Wen, K. Mori, Y. Kuwahara, T. An, H. Yamashita, Appl. Catal. B 218 (2017) 555–569.
- [7] W. Zhao, Y. Huang, Y. Liu, L. Cao, F. Zhang, Y. Guo, B. Zhang, Chem. Eur. J. 22 (2016) 15049–15057.
- [8] M. Wen, K. Mori, Y. Kuwahara, H. Yamashita, ACS Energy Lett. 2 (2017) 1–7.
- [9] D.A. Bulushev, M. Zacharska, E.V. Shlyakhova, A.L. Chuvilin, Y. Guo, S. Beloshapkin, A.V. Okotrub, L.G. Bulusheva, ACS Catal. 6 (2016) 681–691.
- [10] D.A. Bulushev, M. Zacharska, A.S. Lisitsyn, O.Y. Podyacheva, F.S. Hage, Q.M. Ramasse, U. Bangert, L.G. Bulusheva, ACS Catal. 6 (2016) 3442–3451.
- [11] A. Reynal, E. Pastor, M.A. Gross, S. Selim, E. Reisner, J.R. Durrant, Chem. Sci. 6 (2015) 4855–4859.
- [12] G. Papp, G. Olveti, H. Horvath, A. Katho, F. Joo, Dalton Trans. 45 (2016) 14516–14519.
- [13] N. Onishi, M.Z. Ertem, S. Xu, A. Tsurusaki, Y. Manaka, J.T. Muckerman, E. Fujita, Y. Himeda, Catal. Sci. Technol. 6 (2016) 988–992.
- [14] Y.Y. Cai, X.H. Li, Y.N. Zhang, X. Wei, K.X. Wang, J.S. Chen, Angew. Chem. Int. Ed. 52 (2013) 11822–11825.
- [15] Z. Zhang, S.W. Cao, Y. Liao, C. Xue, Appl. Catal. B 162 (2015) 204–209.
- [16] M. Yurderi, A. Bulut, N. Caner, M. Celebi, M. Kaya, M. Zahmakiran, Chem. Commun. 51 (2015) 11417–11420.
- [17] W. Gan, P.J. Dyson, G. Laurenczy, ChemCatChem 5 (2013) 3124–3130.
- [18] A. Boddien, D. Mellmann, F. Gärtnert, R. Jackstell, H. Junge, G.L.P.J. Dyson, R. Ludwig, M. Beller, Science 333 (2011) 1733–1736.
- [19] K. Fujita, R. Kawahara, T. Aikawa, R. Yamaguchi, Angew. Chem. Int. Ed. 54 (2015) 9057–9060.
- [20] W.-H. Wang, M.Z. Ertem, S. Xu, N. Onishi, Y. Manaka, Y. Suna, H. Kambayashi, J.T. Muckerman, E. Fujita, Y. Himeda, ACS Catal. 5 (2015) 5496–5504.
- [21] Q. Liu, X. Yang, Y. Huang, S. Xu, X. Su, X. Pan, J. Xu, A. Wang, C. Liang, X. Wang, T. Zhang, Energy Environ. Sci. 8 (2015) 3204–3207.
- [22] H. Horvath, G. Papp, R. Szabolcsi, A. Katho, F. Joo, ChemSusChem 8 (2015) 3036–3038.
- [23] Q.L. Zhu, N. Tsumori, Q. Xu, J. Am. Chem. Soc. 137 (2015) 11743–11748.
- [24] R.X. Li, X.T. Ren, M.Y. Tang, M.X. Chen, G.B. Huang, C.H. Fang, T. Liu, Z.H. Feng, Y.B. Yin, Y.M. Guo, S.K. Mei, J. Yan, Appl. Catal. B 224 (2018) 772–782.
- [25] D. Kim, D.R. Whang, S.Y. Park, J. Am. Chem. Soc. 138 (2016) 8698–8701.
- [26] J. Tian, Z.Y. Xu, D.W. Zhang, H. Wang, S.H. Xie, D.W. Xu, Y.H. Ren, H. Wang, Y. Liu, Z.T. Li, Nat. Commun. 7 (2016) 11580–11588.
- [27] L. Li, Z. Cai, Q. Wu, W.Y. Lo, N. Zhang, L.X. Chen, L. Yu, J. Am. Chem. Soc. 138 (2016) 7681–7686.
- [28] Y. Chen, S. Zhao, X. Wang, Q. Peng, R. Lin, Y. Wang, R. Shen, X. Cao, L. Zhang, G. Zhou, J. Li, A. Xia, Y. Li, J. Am. Chem. Soc. 138 (2016) 4286–4289.
- [29] S. Pullen, H. Fei, A. Orthaber, S.M. Cohen, S. Ott, J. Am. Chem. Soc. 135 (2013) 16997–17003.
- [30] B. Loges, A. Boddien, H. Junge, J.R. Noyes, W. Baumann, M. Beller, Chem. Commun. 0 (2009) 4185–4187.
- [31] A. Boddien, B. Loges, F. Gartner, C. Torborg, K. Fumino, H. Junge, R. Ludwig, M. Beller, J. Am. Chem. Soc. 132 (2010) 8924–8934.
- [32] K.J. Watson, R. Ziessel, Inorg. Chim. Acta 197 (1992) 125–127.
- [33] S.M. Barrett, S.A. Slattery, A.J.M. Miller, ACS Catal. 5 (2015) 6320–6327.
- [34] X. Liu, X.B. Li, Z. Guan, J. Liu, J. Zhao, Y. Yang, Q.H. Yang, Chem. Commun. 47 (2011) 8073–8075.
- [35] X. Liu, Y. Goto, Y. Maegawa, T. Ohsuna, S. Inagaki, APL Mater. 2 (2014) 113308–113314.
- [36] S. Zhang, H. Wang, M. Li, J. Han, X. Liu, J. Gong, Chem. Sci. 8 (2017) 4489–4496.
- [37] S. Zhang, H. Wang, M. Li, J. Han, S. Inagaki, X. Liu, Dalton Trans. 46 (2017) 9369–9374.
- [38] S. Zhang, H. Wang, L. Tang, M. Li, J. Tian, Y. Cui, J. Han, X. Zhu, X. Liu, Appl. Catal. B 220 (2018) 303–313.
- [39] M. Mandal, M. Kruk, Chem. Mater. 24 (2012) 123–132.
- [40] Z. Dai, Q. Sun, X. Liu, L. Guo, J. Li, S. Pan, C. Bian, L. Wang, X. Hu, X. Meng, L. Zhao, F. Deng, F.S. Xiao, ChemSusChem 10 (2017) 1186–1192.
- [41] H. Hu, Z. Jiao, J. Ye, G. Lu, Y. Bi, Nano Energy 8 (2014) 103–109.
- [42] S. Li, H. Hu, Y. Bi, J. Mater. Chem. A 4 (2016) 796–800.
- [43] P. Xiao, D. Wu, W.H. Fang, G. Cui, Catal. Sci. Technol. 7 (2017) 2763–2771.